

Ubiquitous argonium (ArH^+) in the diffuse interstellar medium: A molecular tracer of almost purely atomic gas

P. Schilke¹, D. A. Neufeld², H. S. P. Müller¹, C. Comito¹, E. A. Bergin³, D. C. Lis^{4,5}, M. Gerin⁶, J. H. Black⁷,
M. Wolfire⁸, N. Indriolo², J. C. Pearson⁹, K. M. Menten¹⁰, B. Winkel¹⁰, Á. Sánchez-Monge¹, T. Möller¹,
B. Godard⁶, and E. Falgarone⁶

¹ I. Physikalisches Institut der Universität zu Köln, Zùlpicher Str. 77, 50937 Köln, Germany
e-mail: schilke@ph1.uni-koeln.de

² The Johns Hopkins University, Baltimore, MD 21218, USA

³ Department of Astronomy, The University of Michigan, 500 Church Street, Ann Arbor, MI 48109-1042, USA

⁴ California Institute of Technology, Pasadena, CA 91125, USA

⁵ Sorbonne Universités, Université Pierre et Marie Curie, Paris 6, CNRS, Observatoire de Paris, UMR 8112 LERMA, Paris, France

⁶ LERMA, CNRS UMR 8112, Observatoire de Paris & École Normale Supérieure, 24 rue Lhomond, 75005 Paris, France

⁷ Department of Earth and Space Sciences, Chalmers University of Technology, Onsala Space Observatory, 439 92 Onsala, Sweden

⁸ Astronomy Department, University of Maryland, College Park, MD 20742, USA

⁹ Jet Propulsion Laboratory, California Institute of Technology, Pasadena, CA 91109, USA

¹⁰ Max-Planck-Institut für Radioastronomie, Auf dem Hügel 69, 53121 Bonn, Germany

Received 28 February 2014 / Accepted 29 March 2014

ABSTRACT

Aims. We describe the assignment of a previously unidentified interstellar absorption line to ArH^+ and discuss its relevance in the context of hydride absorption in diffuse gas with a low H_2 fraction. The confidence of the assignment to ArH^+ is discussed, and the column densities are determined toward several lines of sight. The results are then discussed in the framework of chemical models, with the aim of explaining the observed column densities.

Methods. We fitted the spectral lines with multiple velocity components, and determined column densities from the line-to-continuum ratio. The column densities of ArH^+ were compared to those of other species, tracing interstellar medium (ISM) components with different H_2 abundances. We constructed chemical models that take UV radiation and cosmic ray ionization into account.

Results. Thanks to the detection of two isotopologues, $^{36}\text{ArH}^+$ and $^{38}\text{ArH}^+$, we are confident about the carrier assignment to ArH^+ . NeH^+ is not detected with a limit of $[\text{NeH}^+]/[\text{ArH}^+] \leq 0.1$. The derived column densities agree well with the predictions of chemical models. ArH^+ is a unique tracer of gas with a fractional H_2 abundance of 10^{-4} – 10^{-3} and shows little correlation to H_2O^+ , which traces gas with a fractional H_2 abundance of ≈ 0.1 .

Conclusions. A careful analysis of variations in the ArH^+ , OH^+ , H_2O^+ , and HF column densities promises to be a faithful tracer of the distribution of the H_2 fractional abundance by providing unique information on a poorly known phase in the cycle of interstellar matter and on its transition from atomic diffuse gas to dense molecular gas traced by CO emission. Abundances of these species put strong observational constraints upon magnetohydrodynamical (MHD) simulations of the interstellar medium, and potentially could evolve into a tool characterizing the ISM. Paradoxically, the ArH^+ molecule is a better tracer of almost purely atomic hydrogen gas than HI itself, since HI can also be present in gas with a significant molecular content, but ArH^+ singles out gas that is $>99.9\%$ atomic.

Key words. astrochemistry – line: identification – molecular processes – ISM: abundances – ISM: molecules – ISM: structure

1. Introduction

Light hydrides of the type ZH_n or ZH_n^+ are important diagnostics of the chemical and physical conditions in space. Their lower energy rotational transitions occur for the most part at terahertz frequencies (far-infrared wavelengths). This frequency region can only be accessed to a limited extent from the ground, even at elevated sites, because of strong atmospheric absorptions of H_2O and, to a lesser degree, O_2 and other molecules. The *Herschel* Space Observatory (Pilbratt et al. 2010) has provided a powerful new probe of the submillimeter and far-infrared spectral regions, which greatly expands upon the capabilities afforded

by earlier missions, such as the *Kuiper* Airborne Observatory (KAO; Cameron 1976), the Infrared Space Observatory (ISO; Kessler et al. 1996), and others, or from ground with the Caltech Submillimeter Observatory (CSO; Phillips 1990) or the Atacama Pathfinder EXperiment (APEX; Güsten et al. 2006).

Observations of hydride molecules, in particular of H_2O , in interstellar space, but also in solar system objects, were among the important goals of the *Herschel* mission. In fact, the cationic hydrides H_2O^+ (Ossenkopf et al. 2010), H_2Cl^+ (Lis et al. 2010), and HCl^+ (De Luca et al. 2012) were detected with *Herschel* for the first time in the ISM. While the SH radical has its fundamental transition at a frequency that was inaccessible

to the high-resolution Heterodyne Instrument for Far-Infrared Astronomy (HIFI; de Graauw et al. 2010), it has been detected (Neufeld et al. 2012) with the German REceiver At Terahertz frequencies (GREAT; Heyminck et al. 2012) onboard the Stratospheric Observatory For Infrared Astronomy (SOFIA; Young et al. 2012; Krabbe et al. 2013). OH⁺ (Wyrowski et al. 2010) and SH⁺ (Menten et al. 2011) were detected with APEX from the ground shortly before *Herschel*, but many additional observations were carried out with HIFI, (e.g., Godard et al. 2012). Several hydrides, e.g., OH⁺ and H₂O⁺, were found to be widespread with surprisingly high column densities, not only in Galactic sources (Gerin et al. 2010; Ossenkopf et al. 2010; Neufeld et al. 2010), but also in external galaxies (Weiß et al. 2010; van der Werf et al. 2010; González-Alfonso et al. 2013). As both cations react fast with H₂ to form H₂O⁺ and H₃O⁺, respectively, it was suspected that these molecules reside in mostly atomic gas, which contains little H₂ (Gerin et al. 2010). Detailed model calculations suggest that the abundances of OH⁺ and H₂O⁺ are particularly high in gas with molecular fraction of around 0.05 to 0.1 (Neufeld et al. 2010; Hollenbach et al. 2012). The comparatively high column densities observed for these two molecular cations also require cosmic ray ionization rates in the diffuse ISM to be considerably higher than that in the dense ISM (Neufeld et al. 2010; Hollenbach et al. 2012; Indriolo et al. 2012). However, evidence for high ionization rates in the diffuse ISM, in the range 10⁻¹⁶–10⁻¹⁵ s⁻¹, has been presented already earlier to explain the amount of H₃⁺ in the diffuse ISM (McCall et al. 1998; Liszt 2003; Indriolo & McCall 2012). Even higher cosmic ray ionization rates were estimated for active galaxies such as NGC 4418 and Arp 220 (González-Alfonso et al. 2013, >10⁻¹³ s⁻¹).

Spectral line surveys of the massive and very luminous Galactic Center sources Sagittarius B2(M) and (N) were carried out across the entire frequency range of HIFI within the guaranteed time key project HEXOS, (Bergin et al. 2010). A moderately strong absorption feature was detected toward both sources near 617.5 GHz, but the carrier proved very difficult to assign (Schilke et al. 2010; Müller et al. 2013). This feature appears at all velocity components associated with diffuse, foreground gas, but is conspicuously absent at velocities related to the sources themselves, suggesting that the carrier resides only in very diffuse gas. The absorption line was detected toward other continuum sources as well during subsequent dedicated observations (within the guaranteed time key project PRISMAS; Gerin et al. 2010; Müller et al. 2013).

Very recently, Barlow et al. (2013) observed a line in emission at the same frequency toward the Crab Nebula supernova remnant, which they assigned to the $J = 1-0$ transition of argonium ³⁶ArH⁺ at 617.525 GHz. In addition, they observed the $J = 2-1$ transition at 1234.602 GHz. Here we present evidence that ³⁶ArH⁺ is also responsible for the absorption features detected in the HEXOS and PRISMAS spectra.

2. Observations

The 617.5 GHz features were first discovered in absorption in the full spectral scans of Sagittarius B2(M)¹ and (N)² carried out between 2010 March and 2011 April using *Herschel*/HIFI, within the framework of the HEXOS guaranteed time key Program. The data presented here have been re-reduced using an improved version of the HIFI pipeline, which results in significantly

lower noise levels in the high-frequency HEB mixer bands. The line survey data have been calibrated with HIPE version 10.0 (Roelfsema et al. 2012) and the resulting double-sideband (DSB) spectra were subsequently reduced using the GILDAS CLASS³ package. Basic data reduction steps included removal of spurious features or otherwise unusable portions of the spectra. The continuum emission was then subtracted from the DSB scans by fitting a low-order polynomial (typically first, in a few cases second order). The continuum-subtracted DSB data were deconvolved (sideband separation through pure χ^2 minimization; Comito & Schilke 2002) to provide a single-sideband (SSB) spectrum for each HIFI band. A linear least squares fit of the subtracted continuum values as a function of the LO frequency provided a reliable (unaffected by spectral features) parametrization of the continuum variability across each HIFI band, which was then folded back into the deconvolved, continuum-subtracted SSB spectra. Finally, the overall Sagittarius B2(M) and (N) continuum was rendered self-consistent in two steps: the first adjustment consisted of an additive factor for each band, to achieve a zero-continuum level for the saturated absorption features; the second adjustment required a multiplicative factor, in order for the continuum values in overlap regions between bands to be consistent with one another.

3. Spectroscopy

The noble gas hydride cations NgH⁺, with Ng heavier than helium, are isoelectronic with the hydrogen halides HX; HeH⁺ is isoelectronic with H₂ with ¹ Σ^+ ground electronic states. All non-radioactive noble gas hydride cations have been thoroughly characterized both spectroscopically and kinetically.

On Earth, ⁴⁰Ar is an isotopic abundance of 99.6% is by far the dominant isotope (Berglund & Wieser 2011), but the terrestrial ⁴⁰Ar originates almost exclusively from the radioactive decay of ⁴⁰K. Solar and interstellar argon is dominated by ³⁶Ar (~84.6%), followed by ³⁸Ar (~15.4%), with only traces of ⁴⁰Ar (~0.025%) (Wieler 2002).

3.1. Rest frequencies

Rest frequencies of ³⁶ArH⁺, ³⁸ArH⁺, and ²⁰NeH⁺ (which was in the frequency range of the survey) were taken from the Cologne Database for Molecular Spectroscopy (CDMS, Müller et al. 2001, 2005)⁴. Extensive rotational and rovibrational data were critically evaluated and combined in one global fit for either molecular cation taking the breakdown of the Born-Oppenheimer approximation into account.

The most important spectroscopic data in the case of ArH⁺ are the measurements of rotational transitions of ⁴⁰ArH⁺ (Brown et al. 1988; Liu et al. 1987) and of the $J = 1-0$ transitions of ³⁶ArD⁺, ³⁸ArD⁺, and ⁴⁰ArD⁺ (Bowman et al. 1983). Additional data comprise further rotational transition frequencies of ⁴⁰ArD⁺ (Odashima et al. 1999), as well as rovibrational data of ⁴⁰ArH⁺ (Brault & Davis 1982; Johns 1984), ³⁶ArH⁺, and ³⁸ArH⁺ (Filgueira & Blom 1988), and of ⁴⁰ArD⁺ (Johns 1984). Very recently, Cueto et al. (2014) reported rovibrational transition frequencies, which were rather accurate by infrared standards (~3–4 MHz), but only of modest accuracy by microwave standards. Inclusion of these data, therefore, did not change the frequencies and uncertainties significantly.

¹ *Herschel* OBSIDs: 1342191565.

² *Herschel* OBSIDs: 1342206364.

³ <http://www.iram.fr/IRAMFR/GILDAS>

⁴ <http://www.astro.uni-koeln.de/cdms/>

Table 1. Mapping of location in the Galaxy to velocity regions and color coding toward SgrB2 (see Fig. 4).

Component	v_{LSR} (km s^{-1})	Color code
Galactic center	-136 to -55	green
Norma arm	-50 to -13	red
Galactic center	-9 to 8	green
Sagittarius arm	12 to 22	blue
Scutum arm	25 to 39	orange
Sagittarius B2	47 to 89	light green

Rotational spectra of $^{20}\text{NeH}^+$, $^{22}\text{NeH}^+$, $^{20}\text{NeD}^+$, and $^{22}\text{NeD}^+$ were published by Matsushima et al. (1998). Additional, mostly rovibrational, data were taken from Wong et al. (1982); Ram et al. (1985); Liu et al. (1987); Civiš et al. (2004). The electric dipole moments of ArH^+ and NeH^+ (2.2 D and 3.0 D, respectively) were taken from quantum chemical calculations (Cheng et al. 2007). Other transition frequencies used in the analysis were taken from the CDMS and JPL (Müller et al. 2001, 2005; Pickett et al. 1998) catalogs. Specifically, the methanimine (H_2CNH) entry, based on Dore et al. (2012), was taken from the CDMS, while the methylamine (CH_3NH_2) entry, based on Ilyushin et al. (2005), was taken from the JPL catalog.

4. Results

We report here the detection of an absorption line we identify with $^{36}\text{ArH}^+(1-0)$ toward a number of strong continuum sources, viz. SgrB2(M) and SgrB2(N) from the HEXOS key Program (Bergin et al. 2010), G34.26+0.15, W31C (G10.62-0.39), W49(N), and W51e, from the PRISMAS key Program (Gerin et al. 2010). These sources are star-forming regions that provide strong continuum background illumination for absorption studies of foreground material. Their being star-forming regions, however opens also the possibility of the background continuum being contaminated by source-intrinsic emission lines. The molecular cation is observed at all velocities corresponding to diffuse molecular clouds on the line of sight toward these sources, but is conspicuously absent (or very weak) at velocities related to the sources themselves. We report also upper limits on the column densities of $^{20}\text{NeH}^+$ toward SgrB2(M) and (N).

In principle, the differential rotation of the Milky Way separates spectral features at different Galactocentric radii into distinct locations in velocity space (see, e.g., Vallée 2008). Table 1 lists the different velocity components detectable along the sight-line to the Galactic Center, with the color referring to Fig. 4. The distance determination and hence the assignment to specific spiral arms is complicated due to the streaming motions in the arms (Reid et al. 2009). Particularly, given the kind of gas the ArH^+ line is tracing (see discussion below), we also have to allow for the possibility of detecting inter-arm gas. The exact location of the Galactic center gas observed toward the SgrB2 sources within the Central Molecular Zone is not easily established, due to the non-circular orbits in the Bar potential (Rodríguez-Fernández & Combes 2008).

Barlow et al. (2013) detected the (1-0) and (2-1) transitions of $^{36}\text{ArH}^+$ in emission toward the Crab Nebula, the remnant of supernova 1054. The OH^+ ion was detected in the same spectra, and both ions are probably excited mainly by warm electrons in the same filaments and knots that show low-ionization atomic

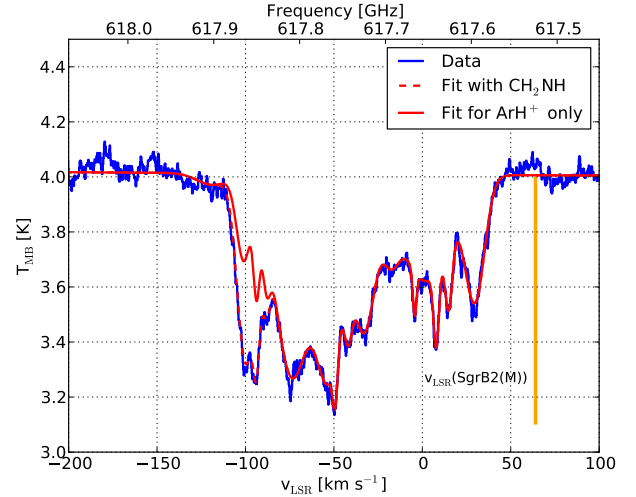


Fig. 1. Spectrum of $^{36}\text{ArH}^+(1-0)$ toward SgrB2(M), with fit including the H_2CNH line blending at -110 km s^{-1} (see Fig. 3) as a dashed red line, and fit of $^{36}\text{ArH}^+$ only in red. Note the lack of absorption at the source velocity 64 km s^{-1} , indicated by the vertical orange marker.

lines in the visible spectrum and H_2 emission lines in the infrared. The conditions in the general ISM we observe, and hence the chemistry, are very different.

In SgrB2(M), we detect only one very wide line, in absorption, which does not absorb at the source intrinsic velocity (see Fig. 1). The breadth of the absorption features introduces a potential uncertainty in the identification, which is definitively resolved by the observation of two different isotopic forms of ArH^+ . Our non-detection of the (2-1) line, which is also covered by the survey, is not surprising, since the molecule possesses a very high dipole moment, thus the transitions have a high critical density, and therefore, in the absence of high density or a very strong FIR field, most of the population will be in the rotational ground state. Fortunately, the $^{38}\text{ArH}^+(1-0)$ line is covered in the observation as well, and, although blended with the $\text{CH}_3\text{OH}(4_{-2,3}-3_{-1,3})$ absorption line, mirrors the absorption pattern of the $^{36}\text{ArH}^+(1-0)$ so closely that we do not have any doubt about the correct identification of the carrier as $^{36}\text{ArH}^+$ (Fig. 2). The fit was conducted with the solar system value of $^{36}\text{Ar}/^{38}\text{Ar} = 5.6$, which seems to reproduce the $^{38}\text{ArH}^+(1-0)$ line well. Both ^{36}Ar and ^{38}Ar are mostly produced in explosive nucleosynthesis through oxygen burning (Woosley et al. 2002).

The $^{36}\text{ArH}^+$ line is blended (at a velocity of about -110 km s^{-1}) with the $\text{H}_2\text{CNH}(2_{2,1}-1_{1,0})$ absorption feature at 617.873 GHz (Fig. 3). The strength of this feature can be estimated, since at 623.292 GHz one finds the $\text{H}_2\text{CNH}(2_{2,0}-1_{1,1})$ line, which is almost identical in excitation and line strength (Fig. 3). However, the $\text{H}_2\text{CNH}(2_{2,0}-1_{1,1})$ line seems to be itself contaminated with the flank of the adjacent $\text{CH}_3\text{NH}_2(9_{2,6}-8_{1,6})$ emission line and thus the absorption could well be underestimated. The strength of the -110 km s^{-1} ArH^+ absorption component should therefore be regarded as a lower limit. The $\text{NeH}^+(1-0)$ line at 1039.3 GHz is also covered by the survey and is not detected. Assuming the same excitation conditions, we get a lower limit of $[\text{ArH}^+]/[\text{NeH}^+] \geq 10$. Although Ne is about 30 times more abundant than Ar, this result is not unexpected, given the different ionization potentials of these species (see Sect. 5).

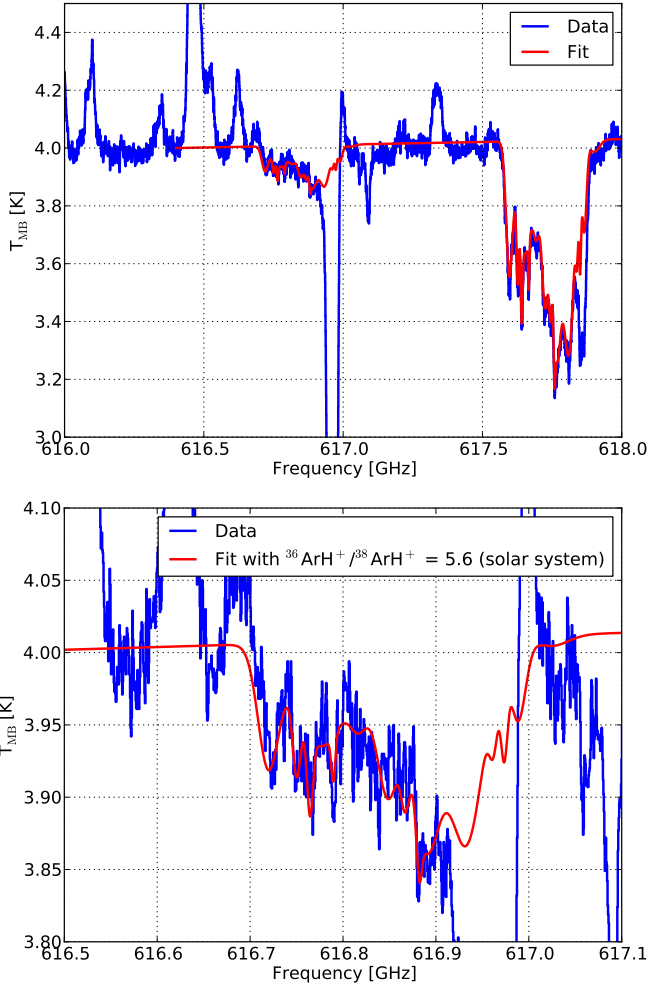


Fig. 2. Spectra with predictions for $^{36}\text{ArH}^+$ and $^{38}\text{ArH}^+$ (top) and zoom in to $^{38}\text{ArH}^+$ (bottom). The $^{38}\text{ArH}^+$ spectrum is scaled from $^{36}\text{ArH}^+$ assuming as $^{36}\text{Ar}/^{38}\text{Ar}$ ratio the solar system value of 5.6.

The column densities were determined using the XCLASS@CASA program⁵ (Möller et al., in prep.), which fits the absorption spectrum with multiple Gaussian components in opacity (hence taking the line shape changes due to opacity into account), assuming an excitation temperature of 2.7 K, using MAGIX (Möller et al. 2013).

In Fig. 4, we show the ArH^+ column density determined in this way, together with the H_2 column density, determined from HF absorption, the H_2O^+ column density, which traces diffuse gas with an H_2/H fraction of 5–10% (Neufeld et al. 2010), atomic hydrogen from Winkel et al. (in prep.), and the ArH^+ abundance relative to atomic hydrogen. The latter is justified by our result from Sect. 5, which shows that ArH^+ traces gas with a H_2/H of $\approx 10^{-3}$. The plots are ordered in descending abundance of the species with respect to H_2 . ArH^+ does not correlate either with molecular gas traced by HF, or the diffuse gas traced by H_2O^+ , which points to different molecular fractions of gas traced by ArH^+ ($f(\text{H}_2) \approx 10^{-3}$) and H_2O^+ ($f(\text{H}_2) \approx 0.1$).

The ArH^+ abundance varies between 3×10^{-8} and 5×10^{-11} , except at very strong HI peaks, and seems to vary smoothly with velocity, with the highest values achieved at the lowest velocities – which however can be affected by the blending with H_2CNH .

⁵ <http://www.astro.uni-koeln.de/projects/schilke/myXCLASSInterface>

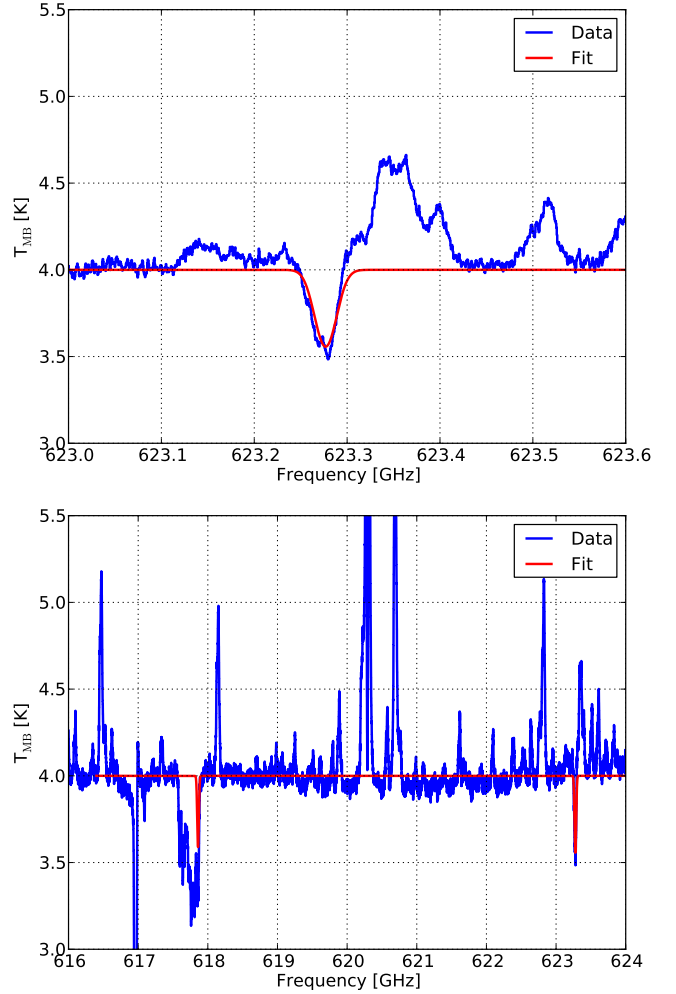


Fig. 3. The $\text{H}_2\text{CNH}(2_{2,0}-1_{1,1})$ line with fit (top) and the two H_2CNH lines (bottom).

Both ArH^+ and H_2O^+ show a distribution in velocity that is more or less continuous and – unlike HF – does not show any breaks associated with the different spiral arm/Galactic Center velocity components. This velocity structure points to the gas responsible for the ArH^+ and H_2O^+ not only tracing spiral arms, but a more continuous mass distribution including interarm gas, which appears to be less molecular (Sawada et al. 2012a,b).

In Fig. 5, we show the fit toward SgrB2(N). It morphologically looks very different from that toward SgrB2(M), which opens the exciting possibility to study the variation of the ArH^+ column density between two nearby lines-of-sight, as have been seen for H_3O^+ toward the same sightlines (Lis et al. 2014). However, there is still contamination by emission lines from the background source, which is more pronounced for SgrB2(N) than for SgrB2(M). An investigation of all emission lines from the survey, which is planned, would enable us to predict the background source emission, and therefore the variation of ArH^+ . At present, however, this investigation has not yet been completed, and in the absence of solid evidence we take the prudent approach of assuming that most of the variations are due to emission line contamination.

In Figs. 6 and 7 we show the data obtained toward the PRISMAS sources G34.25+0.15, W31C (G10.6), W49N, and W51e, together with ArH^+ and H column densities (Winkel et al., in prep.) and ArH^+ abundances relative to H. ArH^+ is weak or absent toward the source envelopes. In the following,

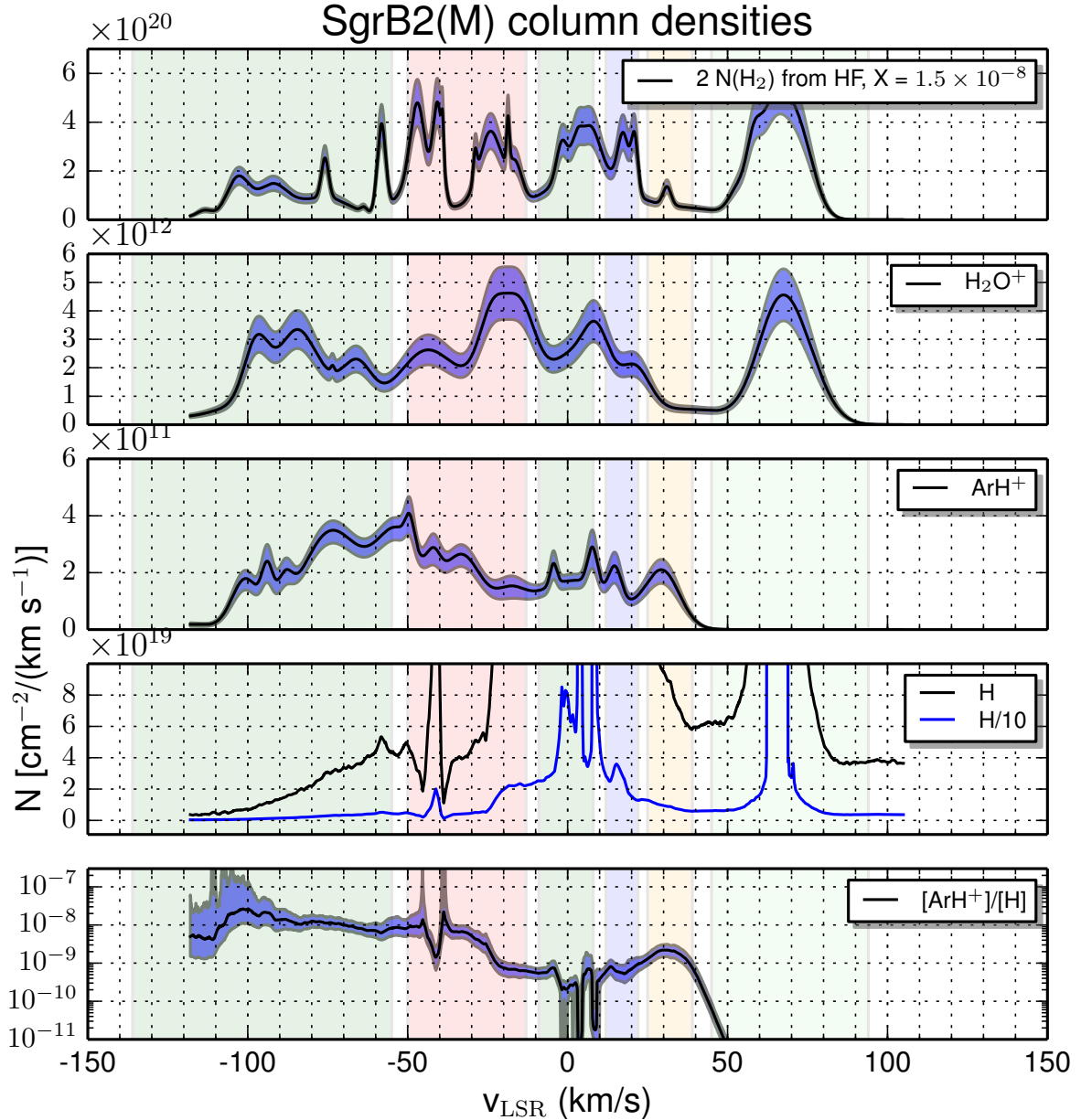


Fig. 4. Column density per km s^{-1} of HF, H_2O^+ , ArH^+ , and H, in descending order of $f(\text{H}_2)$ traced by the species. The color coding of the frequencies is explained in Table 1. The error estimate for ArH^+ was done using the MAGIX Interval Nested Sampling algorithm (Möller et al. 2013), which implements a Markov chain Monte Carlo (MCMC) method to calculate the Bayesian evidence and Bayesian confidence interval. HI column density errors were calculated by propagating uncertainties from the input emission and absorption spectra using a Monte-Carlo sampling technique. For the other species, a $\pm 20\%$ error of the column densities was assumed. The uncertainty is marked by the blue shading around the curves.

we briefly describe the individual sources, following the discussion in Godard et al. (2012) and Flagey et al. (2013).

G34.26+0.15: has a source intrinsic velocity of $v_{\text{LSR}} = 58 \text{ km s}^{-1}$. The ArH^+ absorption at $\approx 60 \text{ km s}^{-1}$ is associated with a strong absorption feature tracing infalling material. Foreground gas is detected at velocities between 0 and 45 km s^{-1} .

W31C: has a source intrinsic velocity of $v_{\text{LSR}} = -2 \text{ km s}^{-1}$. Foreground gas is detected between ≈ 10 and 50 km s^{-1} . The strongest feature appears at 40 km s^{-1} , at the same velocity as H_3O^+ absorption. There could be a weak and broad ArH^+ absorption associated with this source.

W49N: has a source intrinsic velocity of $v_{\text{LSR}} = 10 \text{ km s}^{-1}$. This sight-line presents the strongest ArH^+ absorption outside the Galactic center. Given the large distance (11.4 kpc), the line of sight crosses two spiral arms. The absorption is stronger in the 65 km s^{-1} feature, associated with the Sagittarius spiral arm. The weak absorption near 10 km s^{-1} may be associated with W49 itself.

W51e: has a source intrinsic velocity of $v_{\text{LSR}} = 57 \text{ km s}^{-1}$. Foreground absorption appears between 0 and 45 km s^{-1} and there is a deep absorption near 65 km s^{-1} associated with an infalling layer in the W51 complex. The gas near 22 km s^{-1} is prominent in CH^+ and C^+ , not in molecular lines but shows

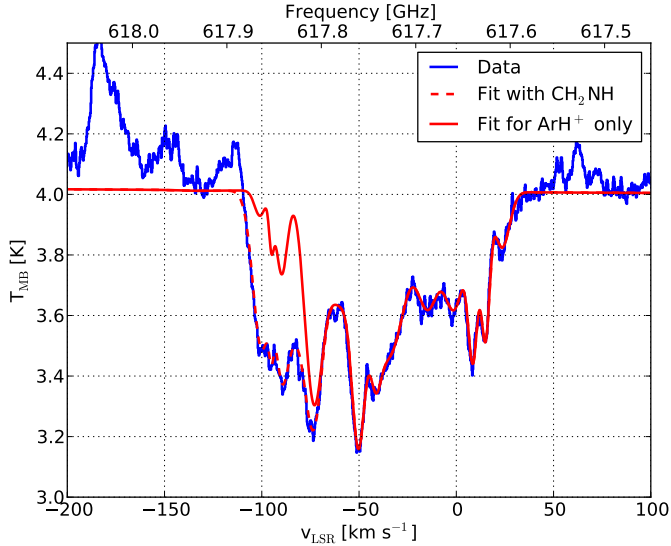


Fig. 5. Fit of SgrB2(N). The $\text{H}_2\text{CNH}(2_{2,0}-1_{1,1})$ lines (here with the additional 80 km s^{-1} component) has been taken out the same way as for SgrB2(M). There has been no correction for emission lines from the background source, which most likely distort the absorption profile.

up weakly in HF and H_2O . Some of the HI signal could be associated with the outflow in W51e.

The spectra also show that there is no very tight correlation with the gas traced by OH^+ and H_2O^+ . The ArH^+ abundances relative to H are similar to those measured on the SgrB2 sight-lines, viz. 3×10^{-9} and 10^{-11} . The HI data toward all sources have some high column density spikes that are probably artifacts related to high opacity regions and the corresponding ArH^+ abundance should be disregarded. The continuity of the ArH^+ absorption and the large width may indicate that some features are associated with the interarm gas.

5. Chemistry of argon in diffuse interstellar clouds

5.1. Basic features of argon chemistry

The interstellar chemistry of the element argon shows several noteworthy features that we list below.

- 1) The ionization potential of atomic argon, $\text{IP}(\text{Ar}) = 15.76 \text{ eV}$, is greater than that of hydrogen, $\text{IP}(\text{H}) = 13.5986 \text{ eV}$. As a result, argon is shielded from ultraviolet radiation capable of ionizing it, and is primarily neutral in the cold neutral medium.
- 2) The proton affinity of argon, $\text{PA}(\text{Ar}) = 369 \text{ kJ mol}^{-1}$ (Hunter & Lias 1998), is smaller than that of molecular hydrogen, $\text{PA}(\text{H}_2) = 422 \text{ kJ mol}^{-1}$. As a result, proton transfer from H_3^+ to Ar is endothermic, with an endothermicity equivalent to 6400 K (Villinger et al. 1982). Moreover, the argonium ion, ArH^+ , can be destroyed by means of an exothermic proton transfer to H_2 , as well to other neutral species with proton affinities greater than that of Ar: these include C, N, CO, and O (Rebrion et al. 1989; Bedford & Smith 1990). Most importantly, however, the proton affinity of Ar is larger than that of atomic hydrogen: thus, ArH^+ is not destroyed by reaction with atomic hydrogen in the cold diffuse medium.
- 3) The ionization potential of atomic argon, $\text{IP}(\text{Ar}) = 15.76 \text{ eV}$, is smaller than $\text{IP}(\text{H}) + D_0(\text{H}_2) = 18.09 \text{ eV}$, where $D_0(\text{H}_2) = 4.48 \text{ eV}$ is the dissociation energy of H_2 . As a result, the dissociative charge transfer reaction $\text{Ar}^+ + \text{H}_2 \rightarrow \text{Ar} + \text{H} + \text{H}^+$ is

Table 2. Reaction list.

Reaction	Assumed rate or rate coefficient	Notes
$\text{Ar} + \text{CR} \rightarrow \text{Ar}^+ + \text{e}$	$(10 + 3.85\phi)\zeta_p(\text{H})$	(1)
$\text{Ar} + \text{H}_2^+ \rightarrow \text{Ar}^+ + \text{H}_2$	$10^{-9} \text{ cm}^3 \text{ s}^{-1}$	(2)
$\text{Ar} + \text{H}_3^+ \rightarrow \text{ArH}^+ + \text{H}_2$	$8 \times 10^{-10} \exp(-6400 \text{ K}/T) \text{ cm}^3 \text{ s}^{-1}$	(3)
$\text{Ar}^+ + \text{e} \rightarrow \text{Ar} + \text{h}\nu$	$3.7 \times 10^{-12} (T/300 \text{ K})^{-0.651} \text{ cm}^3 \text{ s}^{-1}$	(4)
$\text{Ar}^+ + \text{PAH}^- \rightarrow \text{Ar} + \text{PAH}$	$6.8 \times 10^{-8} (T/300 \text{ K})^{-0.5} \text{ cm}^3 \text{ s}^{-1}$	(5)
$\text{Ar}^+ + \text{PAH} \rightarrow \text{Ar} + \text{PAH}^+$	$5.9 \times 10^{-9} \text{ cm}^3 \text{ s}^{-1}$	(5)
$\text{Ar}^+ + \text{H}_2 \rightarrow \text{ArH}^+ + \text{H}$	$8.4 \times 10^{-10} (T/300 \text{ K})^{0.16} \text{ cm}^3 \text{ s}^{-1}$	(6)
$\text{ArH}^+ + \text{H}_2 \rightarrow \text{Ar} + \text{H}_3^+$	$8 \times 10^{-10} \text{ cm}^3 \text{ s}^{-1}$	(3)
$\text{ArH}^+ + \text{CO} \rightarrow \text{Ar} + \text{HCO}^+$	$1.25 \times 10^{-9} \text{ cm}^3 \text{ s}^{-1}$	(3)
$\text{ArH}^+ + \text{O} \rightarrow \text{Ar} + \text{OH}^+$	$8 \times 10^{-10} \text{ cm}^3 \text{ s}^{-1}$	(7)
$\text{ArH}^+ + \text{C} \rightarrow \text{Ar} + \text{CH}^+$	$8 \times 10^{-10} \text{ cm}^3 \text{ s}^{-1}$	(7)
$\text{ArH}^+ + \text{e} \rightarrow \text{Ar} + \text{H}$	$< 10^{-9} \text{ cm}^3 \text{ s}^{-1}$	(8)
$\text{ArH}^+ + \text{h}\nu \rightarrow \text{Ar}^+ + \text{H}$	$1.0 \times 10^{-11} \chi_{\text{UV}} f_A \text{ s}^{-1}$	(9)

Notes. ⁽¹⁾ Kingdon (1965), Jenkins (2013); ϕ is the number of secondary ionizations of H per primary cosmic ray ionization: we adopt the fit given by Dalgarno et al. (1999). ⁽²⁾ Estimate. ⁽³⁾ Villinger et al. (1982). ⁽⁴⁾ Shull & van Steenberg (1982). ⁽⁵⁾ Hollenbach et al. (2012), scaled by reduced mass^{-0.5}. ⁽⁶⁾ Rebrion et al. (1989); Bedford & Smith (1990). ⁽⁷⁾ Assumed equal to the rate for reaction with H_2 . ⁽⁸⁾ Mitchell et al. (2005b). ⁽⁹⁾ Unshielded rate based on theoretical cross-sections of Alexseyev et al. (2007). Attenuation factor $f_A = [E_2(3.6A_V) + E_2(3.6[A_V(\text{tot}) - A_V])]/2$, where E_2 is an exponential integral. (Based on attenuation factor obtained by NW09 for photoionization of Cl.)

endothermic and negligibly slow at the temperature of diffuse interstellar clouds. Thus, in the reaction of Ar^+ and H_2 , the primary product channel leads to the formation of ArH^+ via the H atom abstraction reaction $\text{Ar}^+ + \text{H}_2 \rightarrow \text{ArH}^+ + \text{H}$. This thermochemistry is different from that of the more abundant noble gas elements He and Ne, which have ionization potentials (24.5874 eV and 21.5645 eV respectively) in excess of $\text{IP}(\text{H}) + D_0(\text{H}_2)$; those elements do not efficiently form a hydride cation through reaction of their cation with H_2 , because the product channel is dominated by dissociative charge transfer.

- 4) Dissociative recombination (DR) of ArH^+ (i.e., $\text{ArH}^+ + \text{e} \rightarrow \text{Ar} + \text{H}$) is unusually slow. While almost all diatomic molecular ions, including HeH^+ and NeH^+ (Takagi 2004; Mitchell et al. 2005a), undergo rapid dissociative recombination (DR) at the temperatures of diffuse clouds ($\lesssim 100 \text{ K}$) – with typical rate coefficients $\sim 10^{-7} \text{ cm}^3 \text{ s}^{-1}$ – recent storage ring measurements of the DR of ArH^+ have found the process too slow to measure at energies below 2.5 eV (Mitchell et al. 2005b). While peaks in the DR cross-section have been found at electron energies of 7.5, 16, and 26 eV, and are readily understood with reference to the potential energy curves for ArH^+ , these higher energies are not relevant in cold interstellar gas clouds. Thus, the experimental data place an upper limit of $10^{-9} \text{ cm}^3 \text{ s}^{-1}$ on the DR rate coefficient at interstellar temperatures.
- 5) The photodissociation rate for ArH^+ is unusually small. At wavelengths beyond the Lyman limit (i.e., $> 912 \text{ \AA}$) photodissociation is dominated by transitions to a repulsive $\text{B}^1\Pi$ state, with a vertical excitation energy of 11.2 eV, and to a repulsive $\text{A}^1\Sigma^+$ state, with an excitation energy of 15.8 eV (Alexseyev et al. 2007). The former transition has an unusually small dipole moment (0.13 D), while the latter

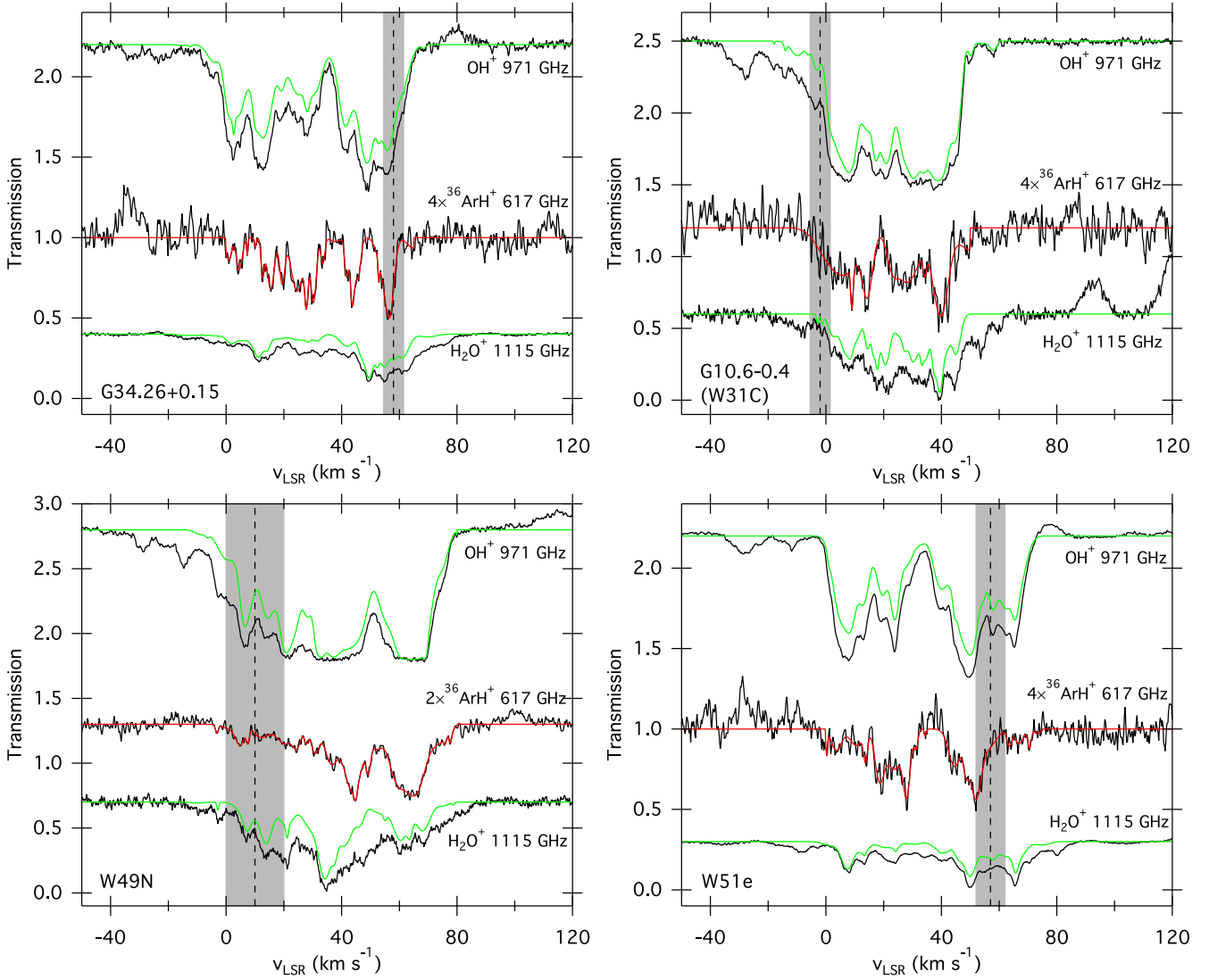


Fig. 6. Observations of OH^+ , H_2O^+ , and ArH^+ toward PRISMAS sources. The green lines for OH^+ and H_2O^+ , whose transitions have hyperfine structure, give the deconvolved strength of the main hyperfine component. The red lines are fits to the ArH^+ spectra used in calculating the column densities presented in Fig. 7. Note that ArH^+ spectra have been scaled up to more clearly show the absorption profiles. Vertical dashed lines and gray shaded regions mark the systemic velocity and velocity dispersion observed for background sources. All OH^+ and H_2O^+ spectra in these sight lines will be presented and analyzed in detail by Indriolo et al. (in prep.). Analyses of OH^+ and H_2O^+ that only utilized a subset of the eventual data have been performed for W31C (Gerin et al. 2010), W49N (Neufeld et al. 2010), and W51 (Wyrowski et al. 2010; Indriolo et al. 2012).

provides a strong absorption feature that has its peak shortward of the Lyman limit. Recent theoretical calculations of the photodissociation cross-section have been performed by Alexseyev et al. (2007) using the multireference Spin-Orbit Configuration Interaction approach. Adopting this cross-section, we estimate a photodissociation rate of only $1.0 \times 10^{-11} \text{ s}^{-1}$ for an unshielded ArH^+ molecule exposed to the mean interstellar radiation field (ISRF) given by Draine (1978). This value is more than two orders of magnitude smaller than that for the isoelectronic HCl molecule (Neufeld & Wolfire 2009). A similar estimate of the ArH^+ photodissociation rate was obtained from the same theoretical cross-sections by Roueff et al. (2014)

- 6) The primary cosmic ray ionization rate for Ar is an order of magnitude larger than that for H (Kingston 1965; Jenkins 2013).

As is always the case in interstellar chemistry (Neufeld & Wolfire 2009; hereafter NW09), basic thermochemical facts (i.e.,

1 through 3 above) play a key role. Clearly, (1) and (2) above are detrimental to the production and survival of argonium in the interstellar medium, while (3) enhances the production rate relative to HeH^+ and NeH^+ . Two unusual features of the kinetics of ArH^+ (4 and 5) enhance its survival in the diffuse ISM, while consideration (6) enhances the production of Ar^+ relative to that of H^+ .

5.2. Diffuse cloud models

In modeling the chemistry of argonium in diffuse molecular clouds, we have modified the diffuse cloud model presented by NW09 and Hollenbach et al. (2012) by the addition of the reactions listed in Table 2. In this reaction network, ArH^+ is produced in a two step process, in which atomic argon undergoes ionization by cosmic rays, and the resultant Ar^+ ion reacts with H_2 to form ArH^+ . ArH^+ is destroyed by photodissociation, or by

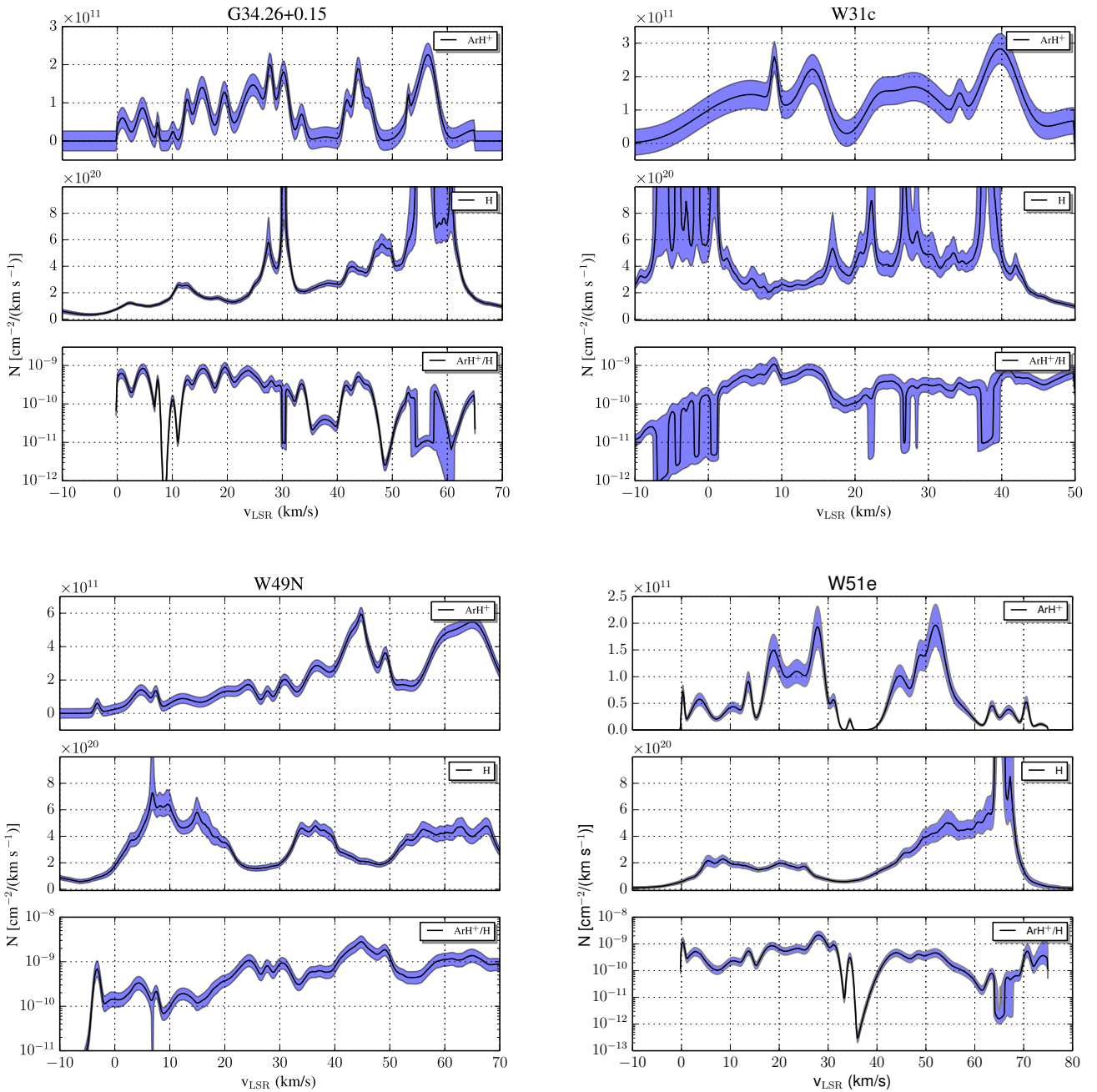


Fig. 7. Column density per km s^{-1} of ArH^+ and H and abundance of ArH^+ relative to H toward the PRISMAS sources. The H column densities come from Winkel et al. (in prep.). The uncertainty is marked by the blue shading around the curves.

transferring a proton to a neutral species (primarily O or H_2) of larger proton affinity than Ar. We note here that in our model we cannot distinguish if the primary ionization is caused by cosmic rays or X-rays, which can play a role in the Galactic center.

In Fig. 8 we show the resultant Ar^+ and ArH^+ abundances for our standard diffuse cloud model. Here, a cloud with an assumed density, n_{H} , of 50 H nuclei per cm^{-3} , is modeled as a slab that is irradiated from both sides by a UV radiation field of intensity equal to that of the mean ISRF (Draine 1978). The assumed primary cosmic ray ionization rate for atomic hydrogen is $\zeta_{\text{p}}(\text{H}) = 2 \times 10^{-16} \text{ s}^{-1}$. Results are shown as a function of depth below the cloud surface, measured in terms of visual

extinction, $A_V = 5.9 \times 10^{-22} N_{\text{H}} \text{ cm}^2 \text{ mag}$ when N_{H} is the column density in cm^{-2} . For the model shown in Fig. 8, the total visual extinction through the slab is $A_V(\text{tot}) = 0.3 \text{ mag}$, and thus the slab midplane is located at $A_V = 0.15 \text{ mag}$.

In Fig. 9, the rates of formation (dashed lines) and destruction (solid lines) by various processes are shown for Ar^+ (upper panel) and ArH^+ (lower panel). The upper panel of Fig. 9 shows that – even close to the cloud surface where the molecular fraction is smallest – the destruction of Ar^+ is dominated by reaction with H_2 to form ArH^+ . Competing pathways, including mutual neutralization with PAH cations, charge transfer with neutral PAHs, and radiative recombination are almost negligible

for molecular hydrogen fractions $\geq 10^{-4}$. Thus, once the molecular fraction exceeds 10^{-4} , more than 75% of Ar ionizations lead to the formation of ArH⁺.

The lower panel of Fig. 9 indicates that the destruction of ArH⁺ is dominated by three processes: proton transfer to H₂, proton transfer to atomic oxygen, and photodissociation. Setting the Ar ionization rate equal to the rate of ArH⁺ destruction via these three processes, we may approximate the predicted ArH⁺ abundance by the equation

$$\frac{n(\text{ArH}^+)}{n(\text{Ar})} = \frac{\zeta(\text{Ar})}{k_1 n(\text{O}) + k_2 n(\text{H}_2) + \zeta_{\text{pd}}(\text{ArH}^+)} \quad (1)$$

where $k_1 = 8 \times 10^{-10} \text{ cm}^3 \text{ s}^{-1}$ is the rate coefficient for proton transfer to H₂, k_2 (assumed equal to k_1) is the rate coefficient for proton transfer to O, and $\zeta_{\text{pd}}(\text{ArH}^+)$ is the photodissociation rate for ArH⁺ (equal to $1.1 \times 10^{-11} \chi_{\text{UV}} \text{ s}^{-1}$ in the limit of no shielding, where χ_{UV} is the intensity of the ISRF in units of the mean Galactic value given by Draine 1978). The numerator in Eq. (1) is the total ionization rate for Ar, which, following Jenkins (2013), we take as $(10 + 3.85\phi)\zeta_{\text{p}}(\text{H})$, where ϕ is the number of secondary ionizations of H per primary ionization. Using the fit to ϕ given by Dalgarno et al. (1999), we find that ϕ ranges from 0.48 to 0.26 within the standard cloud model presented here. Adopting the middle of that range, we find that $\zeta(\text{Ar}) \sim 11.4\zeta_{\text{p}}(\text{H})$.

Now assuming an atomic oxygen abundance of 3.9×10^{-4} relative to H nuclei, and assuming a solar argon abundance of 3.2×10^{-6} (Lodders 2010), we find that Eq. (1) may be rewritten as

$$\frac{n(\text{ArH}^+)}{n_{\text{H}}} = \frac{1.2 \times 10^{-10} \zeta_{\text{p}}(\text{H})_{-16}}{n_2 [1 + 1280 f(\text{H}_2)] + 0.35 \chi_{\text{UV}} \times f_A} \quad (2)$$

where $n_2 = n_{\text{H}}/100 \text{ cm}^{-3}$, $\zeta_{\text{p}}(\text{H})_{-16} = \zeta_{\text{p}}(\text{H})/10^{-16} \text{ s}^{-1}$, $f(\text{H}_2) = 2n(\text{H}_2)/n_{\text{H}}$ is the molecular fraction, and f_A is the factor by which the photodissociation rate for ArH⁺ is reduced by attenuation. For the isotropic illumination that we assume, $f_A = [E_2(3.6 A_V) + E_2(3.6 [A_V(\text{tot}) - A_V])]/2$, where E_2 is an exponential integral; for the $A_V(\text{tot}) = 0.3 \text{ mag}$ model, f_A varies from 0.56 at the cloud surface to 0.30 at the cloud center. Figure 10 shows the Ar⁺ and ArH⁺ abundances as a function of the molecular fraction. For molecular fractions in excess of $\sim 10^{-4}$, Eq. (2) reproduces the exact behavior to within 15%.

While astrochemical models predict molecular abundance ratios as a function of position within a gas cloud, astronomical observations measure column density ratios averaged along the line-of-sight. Accordingly, we have calculated the column-averaged ArH⁺ abundance, $N(\text{ArH}^+)/N_{\text{H}}$, for a series of models with different assumed $A_V(\text{tot})$. In the upper and middle panels of Fig. 11, we plot the $N(\text{ArH}^+)/N_{\text{H}}$ ratio and the average molecular fraction, $2N(\text{H}_2)/N_{\text{H}}$, as a function of $A_V(\text{tot})$, while in the lower panel we show the column-averaged ArH⁺ abundance as a function of molecular fraction. Given the cosmic ray ionization rate $\zeta_{\text{p}}(\text{H}) = 2 \times 10^{-16} \text{ s}^{-1}$ and the gas density $n_{\text{H}} = 50 \text{ cm}^{-3}$ assumed in our standard model, peak $N(\text{ArH}^+)/N_{\text{H}}$ ratios $\sim 2 \times 10^{-10}$ are achieved within small clouds of total visual extinction $\leq 0.01 \text{ mag}$, within which the average molecular fraction is $\leq 10^{-3}$. The predicted peak abundances scale linearly with the assumed cosmic ray ionization rate and, for weak UV fields, inversely with the density. For UV fields higher than $\chi_{\text{UV}} = n_2 [1 + 1200 f(\text{H}_2)] / (0.35 f_A)$, i.e., for $\chi_{\text{UV}} \approx 10 n_2$, photodissociation is the dominant process.

For the standard cosmic ray ionization rates assumed in our diffuse cloud models, the peak ArH⁺ abundances, predicted to

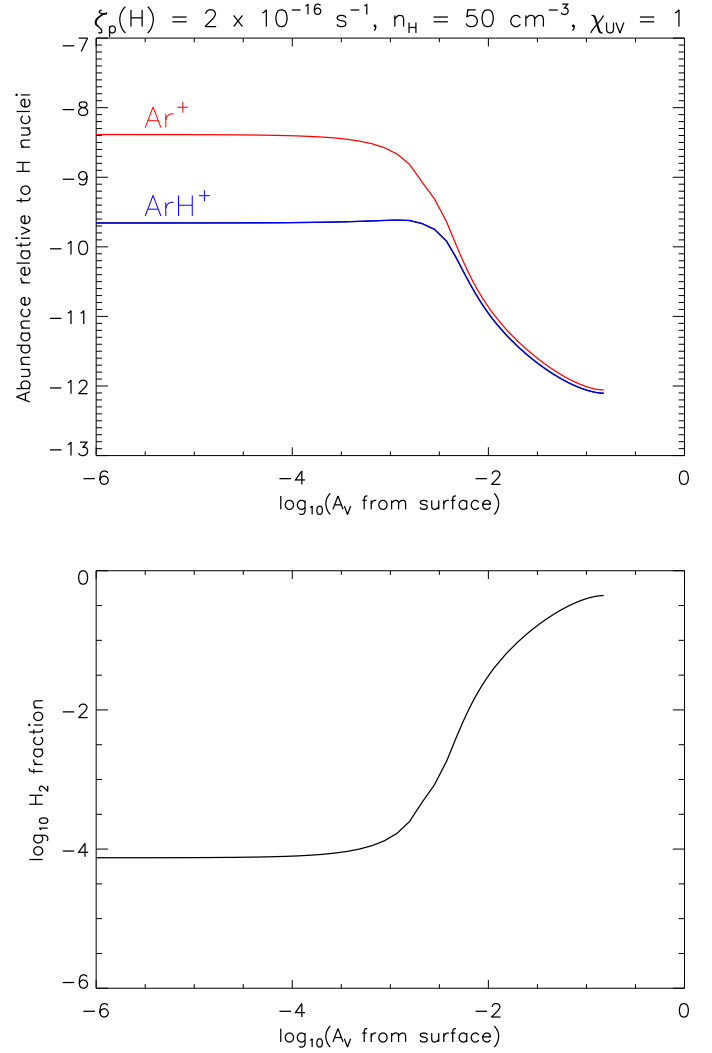


Fig. 8. Abundances of Ar⁺ and ArH⁺ as function of A_V (upper panel) and $f(\text{H}_2)$ (lower panel). The elemental abundance of Ar is 3.2×10^{-6} , so most of the Argon is still neutral.

be $\approx 2 \times 10^{-10}$ relative to H, fall near the lower end of the observed range reported in Sect. 4. Higher observed abundances may indicate local enhancements in the cosmic ray ionization rate. Along the sight-line to Sgr B2 (M), the observed ArH⁺/H ratio is largest for velocities corresponding to X2 orbits in the Galactic Center: these are indeed exactly the cloud velocities for which the largest cosmic ray ionization rate would be expected.

The diffuse cloud models presented in Sect. 5.2 provide a natural explanation for why ArH⁺ is present in the diffuse arm and interarm gas, but absent in the denser gas associated with the background continuum sources: owing to its rapid destruction by H₂, the predicted ArH⁺ abundance falls rapidly once the molecular fraction exceeds $\approx 10^{-3}$. Thus, both theory and observation suggest that argonium is the molecule that paradoxically abhors molecular clouds.

We have also run Turbulent Dissipation Region (TDR; Godard et al. 2009) models, but have found that they predict no significant enhancement of ArH⁺. This is not surprising, since the only endothermic production rate in Table 2, the reaction of H₃⁺ with Ar, is only important in regions of large molecular fraction, where ArH⁺ is rapidly removed. Although we did not find the elevated temperatures due to enhanced viscous dissipation

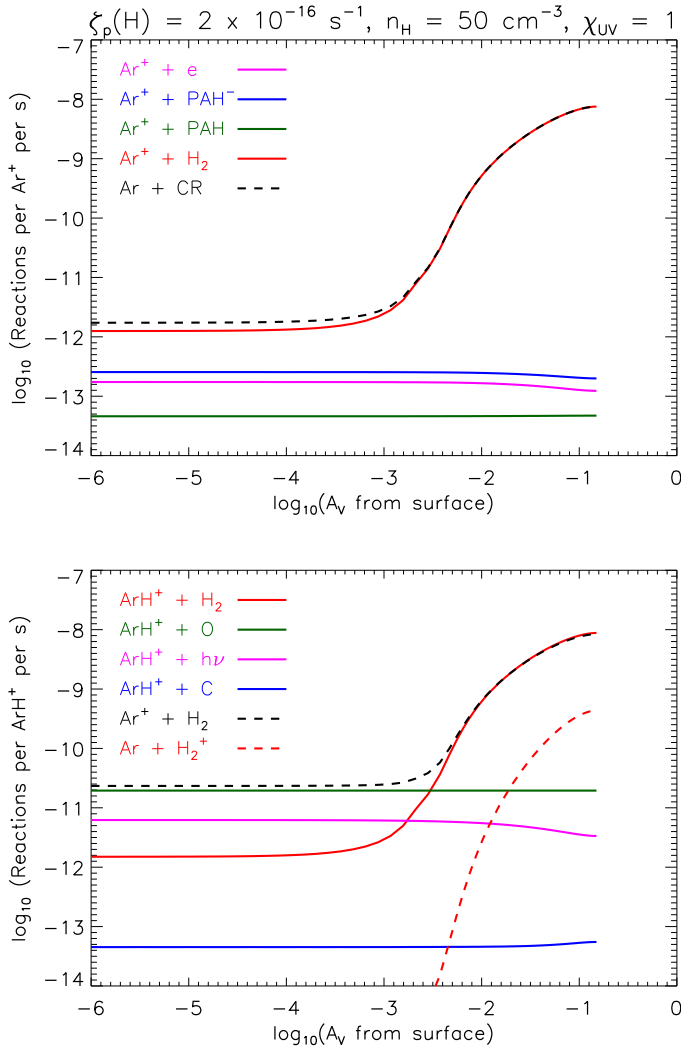


Fig. 9. Rates of formation (dashed lines) and destruction (solid lines) by various processes are shown for Ar^+ (upper panel) and ArH^+ (lower panel).

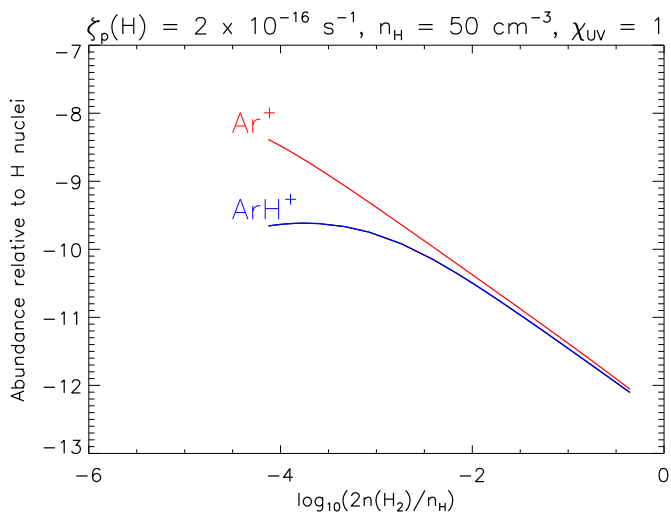


Fig. 10. Same as Fig. 8, except with the Ar^+ and ArH^+ abundances shown as a function of molecular fraction.

and ion-neutral friction in regions of intermittent turbulent dissipation to be important in driving endothermic reactions of

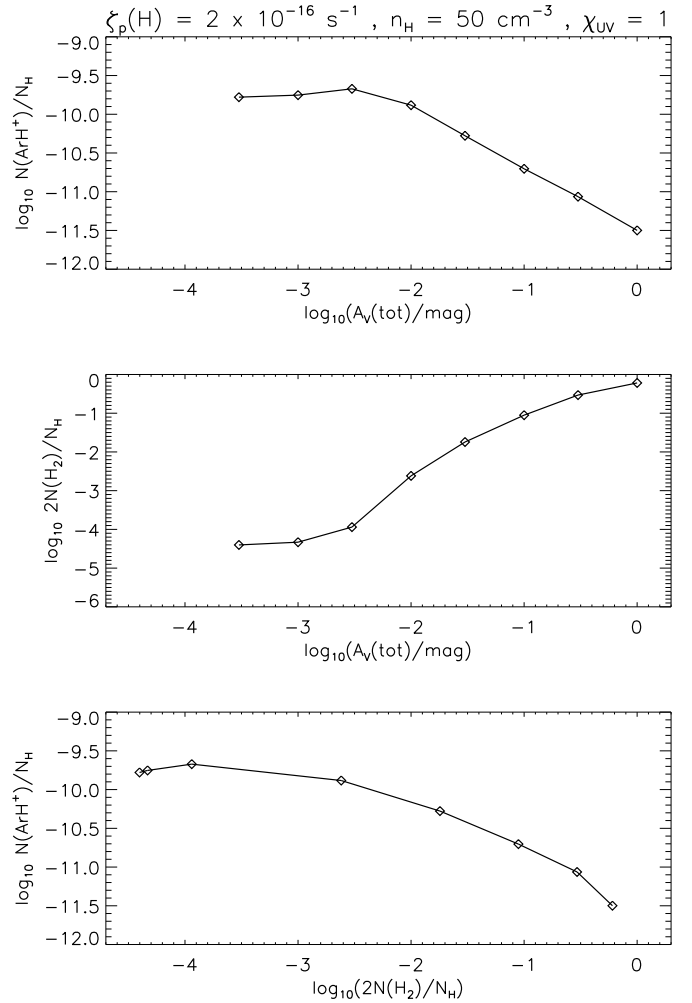


Fig. 11. Column-averaged ArH^+ abundance, $N(\text{ArH}^+)/N_{\text{H}}$ (top panel), and average molecular fraction, $2N(\text{H}_2)/N_{\text{H}}$, as a function of $A_V(\text{tot})$. Bottom panel: column-averaged ArH^+ abundance versus average molecular fraction, $2N(\text{H}_2)/N_{\text{H}}$.

relevance to the production of ArH^+ , these regions are possible sites of cosmic ray acceleration because they are associated with intense current sheets (Momferratos et al. 2014).

6. Summary

We confidently assign the 617.5 GHz line to the carrier $^{36}\text{ArH}^+$, since features of $^{38}\text{ArH}^+$ were also detected toward Sgr B2(M) and (N) with $^{36}\text{Ar}/^{38}\text{Ar}$ ratios close to, but probably smaller than in the solar neighborhood. The line surveys cover the frequency of the $J = 1-0$ transition of $^{20}\text{NeH}^+$ and even though Ne is much more abundant in space than Ar, we do not observe neonium absorption. This difference is in line with expectations based on the much higher ionization potential of Ne.

Our chemical calculations show that ArH^+ can exist only in low-density gas with a low H_2 fraction ($f(\text{H}_2) \approx 10^{-4}-10^{-3}$), and a weak UV field, while an enhanced cosmic ray flux can boost its abundance. OH^+ and H_2O^+ trace gas with a larger H_2 fraction of 0.1, and are therefore complementary probes (Gerin et al. 2010; Neufeld et al. 2010; Hollenbach et al. 2012). It is noteworthy, in this context, that the ArH^+ and H_2O^+ column densities are not well-correlated, although one would assume that ArH^+ and H_2O^+ both trace the stratified PDR structures of diffuse clouds, ArH^+ the very outer edge, and H_2O^+ gas deeper in.

It appears that this picture is too simplistic. The aforementioned tracers OH⁺ and H₂O⁺ trace partly molecular gas, while the so-called CO-dark gas, which is predominantly molecular, but does not contain significant abundances of CO, is best traced by HF, CH, H₂O, or HCO⁺ (Qin et al. 2010; Sonnentrucker et al. 2010; Flagey et al. 2013), but also by [CII] (Langer et al. 2014), which however is not very specific to this component. The careful analysis of column density variations in these tracers promises to disentangle the distribution of the H₂ fraction, providing a direct observational probe on the poorly known transition of primarily atomic diffuse gas to dense molecular gas traced by CO emission, putting strong constraints upon magnetohydrodynamical simulations for the interstellar gas (e.g. Micic et al. 2012; Levrier et al. 2012) and thus potentially evolving into a tool to characterize the ISM. Paradoxically, ArH⁺ actually is a better tracer of almost purely atomic gas than the HI line, because with the column density of H we see gas that could be 0.1%, 1%, or 50% molecular, while ArH⁺ singles out gas which is more than 99.9% atomic.

However, the possibilities of getting more data are limited. While both the 909 GHz OH⁺ line and the 607 GHz *para*-H₂O⁺ line can be observed under very good weather conditions from very good sites on the ground (see, e.g. Wyrowski et al. 2010), ArH⁺, due to its proximity to the 620.7 GHz water line, is extremely difficult even from excellent sites. Receivers covering these frequencies with SOFIA would therefore be highly beneficial. The other possibility to get access to these species are toward redshifted galaxies. There, however, OH⁺ and H₂O⁺ are often seen in emission, indicating very different excitation conditions. ArH⁺ has not been found in extragalactic sources yet, but could be a very good tracer of cosmic rays in diffuse gas with little UV penetration.

Acknowledgements. HIFI has been designed and built by a consortium of institutes and university departments from across Europe, Canada and the United States under the leadership of SRON Netherlands Institute for Space Research, Groningen, The Netherlands and with major contributions from Germany, France and the US. Consortium members are: Canada: CSA, U. Waterloo; France: CESR, LAB, LERMA, IRAM; Germany: KOSMA, MPIfR, MPS; Ireland, NUI Maynooth; Italy: ASI, IFSI-INAF, Osservatorio Astrofisico di Arcetri-INAF; Netherlands: SRON, TUD; Poland: CAMK, CBK; Spain: Observatorio Astronómico Nacional (IGN), Centro de Astrobiología (CSIC-INTA). Sweden: Chalmers University of Technology – MC2, RSS & GARD; Onsala Space Observatory; Swedish National Space Board, Stockholm University – Stockholm Observatory; Switzerland: ETH Zurich, FHNW; USA: Caltech, JPL, NHSC. H.S.P.M. is very grateful to the Bundesministerium für Bildung und Forschung (BMBF) for initial support through project FKZ 500F0901 (ICC HIFI *Herschel*) aimed at maintaining the Cologne Database for Molecular Spectroscopy, CDMS. This support has been administered by the Deutsches Zentrum für Luft- und Raumfahrt (DLR). Part of this work was supported by the German *Deutsche Forschungsgemeinschaft* in the Collaborative Research Center SFB956, and by the German Ministry of Science (BMBF) through contract 05A11PK3. This work also has been supported by NASA through an award issued by JPL/Caltech. We thank Christian Endres for tireless work on the molecular line catalog implementation.

References

Alekseyev, A. B., Liebermann, H.-P., & Buenker, R. J. 2007, *Phys. Chem. Chem. Phys.*, 9, 5088
 Barlow, M. J., Swinyard, B. M., Owen, P. J., et al. 2013, *Science*, 342, 1343
 Bedford, D. K., & Smith, D. 1990, *Intl. J. Mass Spectrom. Ion Process.*, 98, 179
 Bergin, E. A., Phillips, T. G., Comito, C., et al. 2010, *A&A*, 521, L20
 Berglund, M., & Wieser, M. E. 2011, *Pure Appl. Chem.*, 83, 397
 Bowman, W. C., Plummer, G. M., Herbst, E., & de Lucia, F. C. 1983, *J. Chem. Phys.*, 79, 2093
 Brault, J. W., & Davis, S. P. 1982, *Phys. Scr.*, 25, 268

Brown, J. M., Jennings, D. A., Vanek, M., Zink, L. R., & Evenson, K. M. 1988, *J. Mol. Spectrosc.*, 128, 587
 Cameron, R. M. 1976, *Sky Telesc.*, 52, 327
 Civiš, S., Šebera, J., Špirko, V., et al. 2004, *J. Mol. Struct.*, 695, 5
 Cheng, M., Brown, J. M., Rosmus, P., et al. 2007, *Phys. Rev. A*, 75, 012502
 Chin, Y.-N., Henkel, C., Whiteoak, J. B., Langer, N., & Churchwell, E. B. 1996, *A&A*, 305, 960
 Comito, C., & Schilke, P. 2002, *A&A*, 395, 357
 Cueto, M., Cernicharo, J., Barlow, M. J., et al. 2014, *ApJ*, 783, L5
 Dalgarno, A., Yan, M., & Liu, W. 1999, *ApJS*, 125, 237
 de Graauw, T., Helmich, F. P., Phillips, T. G., et al. 2010, *A&A*, 518, L6
 De Luca, M., Gupta, H., Neufeld, D., et al. 2012, *ApJ*, 751, L37
 Dore, L., Bizzocchi, L., & Degli Esposti, C. 2012, *A&A*, 544, A19
 Draine, B. T. 1978, *ApJS*, 36, 595
 Filgueira, R. R., & Blom, C. E. 1988, *J. Mol. Spectrosc.*, 127, 279
 Flagey, N., Goldsmith, P. F., Lis, D. C., et al. 2013, *ApJ*, 762, 11
 Gerin, M., de Luca, M., Black, J., et al. 2006, *A&A*, 454, L13
 Godard, B., Falgarone, E., & Pineau Des Forêts, G. 2009, *A&A*, 495, 847
 Godard, B., Falgarone, E., Gerin, M., et al. 2012, *A&A*, 540, A87
 González-Alfonso, E., Fischer, J., Bruderer, S., et al. 2013, *A&A*, 550, A25
 Güsten, R., Nyman, L. Å., Schilke, P., et al. 2006, *A&A*, 454, L13
 Heyminck, S., Graf, U. U., Güsten, R., et al. 2012, *A&A*, 542, L1
 Hollenbach, D., Kaufman, M. J., Neufeld, D., et al. 2012, *ApJ*, 754, 105
 Hunter, E. P. L., & Lias, S. G. 1998, *J. Phys. Chem. Ref. Data*, 27, 413
 Ilyushin, V. V., Alekseev, E. A., Dyubko, S. F., Motiyenko, R. A., & Hougen, J. T. 2005, *J. Mol. Spectrosc.*, 229, 170
 Indriolo, N., & McCall, B. J. 2012, *ApJ*, 745, 91
 Indriolo, N., Neufeld, D. A., Gerin, M., et al. 2012, *ApJ*, 758, 83
 Jenkins, E. B. 2013, *ApJ*, 764, 25
 Johns, J. W. C. 1984, *J. Mol. Spectrosc.*, 106, 124
 Kessler, M. F., Steinz, J. A., Anderegg, M. E., et al. 1996, *A&A*, 315, L27
 Kingston, A. E. 1965, *Proc. Phys. Soc.*, 86, 467
 Krabbe, A., Mehler, D., Röser, H.-P., & Scorza, C. 2013, *Eur. J. Phys.*, 34, 161
 Langer, W. D., Velusamy, T., Pineda, J. L., Willacy, K., & Goldsmith, P. F. 2014, *A&A*, 561, A122
 Levrier, F., Le Petit, F., Hennebelle, P., et al. 2012, *A&A*, 544, A22
 Lis, D. C., Pearson, J. C., Neufeld, D. A., et al. 2010, *A&A*, 521, L9
 Lis, D. C., Schilke, P., Bergin, E. A., et al. 2014, *ApJ*, 785, 135
 Liszt, H. 2003, *A&A*, 398, 621
 Liu, D.-J., Ho, W.-C., & Oka, T. 1987, *J. Chem. Phys.*, 87, 2442
 Matsushima, F., Ohtaki, Y., Torige, O., & Takagi, K. 1998, *J. Chem. Phys.*, 109, 2242
 McCall, B. J., Geballe, T. R., Hinkle, K. H., & Oka, T. 1998, *Science*, 279, 1910
 Menten, K. M., Wyrowski, F., Belloche, A., et al. 2011, *A&A*, 525, A77
 Micic, M., Glover, S. C. O., Federrath, C., & Klessen, R. S. 2012, *MNRAS*, 421, 2531
 Mitchell, J. B. A., Novotny, O., Angelova, G., et al. 2005a, *J. Phys. B At. Mol. Phys.*, 38, 693
 Mitchell, J. B. A., Novotny, O., LeGarrec, J. L., et al. 2005b, *J. Phys. B At. Mol. Phys.*, 38, L175
 Möller, T., Bernst, I., Panoglou, D., et al. 2013, *A&A*, 549, A21
 Momferratos G., Lesaffre, P., Falgarone E., & Pineau des Forêts, G. 2014, *MNRAS*, in press
 Müller, H. S. P., Thorwirth, S., Roth, D. A., & Winnewisser, G. 2001, *A&A*, 370, L49
 Müller, H. S. P., Schlöder, F., Stutzki, J., & Winnewisser, G. 2005, *J. Mol. Struct.*, 742, 215
 Müller, H. S. P., Schilke, P., & Gerin, M., et al. 2013, *The Diffuse Interstellar Bands*, *Proc. IAU Symp.*, 297
 Neill, J. L., Bergin, E. A., Lis, D. C., et al. 2012, *J. Mol. Spectrosc.*, 280, 150
 Neufeld, D. A., & Wolfire, M. G. 2009, *ApJ*, 706, 1594 (NW09)
 Neufeld, D. A., Goicoechea, J. R., Sonnentrucker, P., et al. 2010, *A&A*, 521, L10
 Neufeld, D. A., Falgarone, E., Gerin, M., et al. 2012, *A&A*, 542, L6
 Odashima, H., Kozato, A., Matsushima, F., Tsunekawa, S., & Takagi, K. 1999, *J. Mol. Spectrosc.*, 195, 356
 Ossenkopf, V., Müller, H. S. P., Lis, D. C., et al. 2010, *A&A*, 518, L111
 Phillips, T. G. 1990, *Liege International Astrophysical Colloquia*, 29, 291
 Pickett, H. M., Poynter, R. L., Cohen, E. A., et al. 1998, *J. Quant. Spectrosc. Rad. Transf.*, 60, 883
 Pilbratt, G. L., Riedinger, J. R., Passvogel, T., et al. 2010, *A&A*, 518, L1
 Qin, S.-L., Schilke, P., Comito, C., et al. 2010, *A&A*, 521, L14
 Ram, R. S., Bernath, P. F., & Brault, J. W. 1985, *J. Mol. Spectrosc.*, 113, 451
 Rebrion, C., Rowe, B. R., & Marquette, J. B. 1989, *J. Chem. Phys.*, 91, 6142
 Reid, M. J., Menten, K. M., Zheng, X. W., et al. 2009, *ApJ*, 700, 137
 Rodriguez-Fernandez, N. J., & Combes, F. 2008, *A&A*, 489, 115

- Roelfsema, P. R., Helmich, F. P., Teyssier, D., et al. 2012, A&A, 537, A17
- Roueff, E., Alekseyev, A. B., & Le Bourlot, J. 2014, A&A, 566, A30
- Sawada, T., Hasegawa, T., Sugimoto, M., Koda, J., & Handa, T. 2012a, ApJ, 752, 118
- Sawada, T., Hasegawa, T., & Koda, J. 2012b, ApJ, 759, L26
- Schilke, P., HEXOS Team 2010, in Proc. Herschel First Results Symp., http://herschel.esac.esa.int/FirstResultsSymposium/presentations/A34_SchilkeP_SgrB2.pdf
- Schilke, P., Lis, D. C., Bergin, E. A., Higgins, R., & Comito, C. 2013, J. Phys. Chem. A, 117, 9766
- Sonnentrucker, P., Neufeld, D. A., Phillips, T. G., et al. 2010, A&A, 521, L12
- Shull, J. M., & van Steenberg, M. 1982, ApJS, 48, 95
- Takagi, H. 2004, Phys. Rev. A, 70, 022709
- Vallée, J. P. 2008, AJ, 135, 1301
- van der Werf, P. P., Isaak, K. G., Meijerink, R., et al. 2010, A&A, 518, L42
- Villinger, H., Futrell, J. H., Howorka, F., Duric, N., & Lindinger, W. 1982, J. Chem. Phys., 76, 3529
- Weiß, A., Requena-Torres, M. A., Güsten, R., et al. 2010, A&A, 521, L1
- Wieler, R. 2002, Rev. Mineral. Geochim. 47, 21
- Wilson, T. L., & Rood, R. 1995, ARA&A, 32, 191
- Wong, M., Bernath, P., & Amano, T. 1982, J. Chem. Phys., 77, 693
- Woosley, S. E., Heger, A., & Weaver, T. A. 2002, Rev. Mod. Phys., 74, 1015
- Wyrowski, F., Menten, K. M., Güsten, R., & Belloche, A. 2010, A&A, 518, A26
- Young, E. T., Becklin, E. E., Marcum, P. M., et al. 2012, ApJ, 749, L17